# Elastic properties and phonon generation in Mo/Si superlattices

L. Belliard,[1,*] A. Huynh,[1] B. Perrin,[1] A. Michel,[2] G. Abadias,[2] and C. Jaouen[2]

[1]*Institut des NanoSciences de Paris, UMR 7588, CNRS–Université Pierre et Marie Curie, 140 rue de Lourmel, 75015 Paris, France*

[2]*Laboratoire de Physique des Matériaux (PHYMAT), UMR 6630 CNRS, SP2MI, Téléport 2, Boulevard Marie et Pierre Curie,*
*Boîte Postale 30179, 86962 Chasseneuil Cedex, France*

Picosecond ultrasonic measurements have been carried out on molybdenum-silicon multilayers in order to study their elastic effective-medium behavior using low-frequency acoustic echoes, and their high-frequency response through localized surface modes. Taking into account the elastic properties of silicon and molybdenum thin films independently measured, we show that the long-wavelength acoustic behavior of the multilayers is well reproduced. Using an effective-medium model that includes only the two constituent layers in the periodic cell without any interfacial zone, sound velocity, echo shape, and acoustical reflection coefficient have been investigated. In contrast, the frequency of the acoustic-phonon surface modes could not be reproduced unless a modification of the surface silicon layer was introduced, in good agreement with x-ray reflectivity measurements. Finally, low-temperature experiments illustrate the potential of such wide stop-band systems for the emission of monochromatic acoustic waves, using the tunneling of a surface-localized mode or a buried nanocavity mode. The filtering and acoustic transduction properties of these artificial layered materials have also been investigated.

PACS number(s): 68.65.Cd, 63.20.−e

## I. INTRODUCTION

For over 70 years, the propagation of acoustic waves in layered systems has received great attention. Nevertheless, in simulations of seismic shocks the scale of the earth's crust structure was in the kilometer range; today, the technological development to create alternated stackings drives the scale of interest in the nanometer range. In artificial multilayers, the periodicity along the direction perpendicular to the surface strongly modifies the microstructure and the acoustic properties. Among the interesting results, folded modes,[1,2] unexpected softening of the elastic constants,[3] interfacial alloying,[4] and interface roughness have been observed; such superlattice structures have shown promising potential in various fields of application.

For example, molybdenum-silicon (Mo/Si) multilayers with a high contrast in electron density exhibit a very high reflectivity for soft x-rays and extreme UV. They are widely used nowadays in a variety of technological fields such as x-ray laser cavities,[5] soft x-ray lithography,[6] and microscopy.[7] Meanwhile, the large discrepancy in acoustic impedance of the two multilayer components gives rise to large stop bands, which are of technological interest for optimizing acoustic-phonon filters, as they overcome some of the drawbacks of semiconductor superlattices.[8] Special attention has to be given to the interface quality for the mirrors; the interfaces should be as abrupt as possible and without residual strains. Different fabrication processes have been investigated, and magnetron sputtering seems to be the most efficient regarding the optimization of the optical properties of multilayers.[9]

Picosecond ultrasonics is nowadays considered as a powerful technique to study the acoustic behavior of multilayer systems. Femtosecond laser excitations allow the generation of high-frequency acoustic waves with wavelengths in the nanometer range. Such acoustical strains traveling into a layered system and interacting with all the sample interfaces strongly interact with the acoustical features of the buried structures. Previous acoustical studies of Mo/Si multilayers have shown the existence of folded modes due to the multilayer periodicity. Moreover, nonpropagating modes have been detected within band gaps as far as the sixth band gap of the dispersion curves. Nevertheless, the discrepancy between theoretical and experimental values of the frequency of such surface-localized modes can reach around 20%, a difference that could be related to the ill-known elastic constants of the constituent materials.[10–13]

In this paper, time-resolved picosecond acoustic measurements on a series of Mo/Si multilayers with thickness periods $d$ ranging from 4.6 up to 28.4 nm are presented. The structural and acoustic properties of each constituent layer were obtained separately on single-layer reference samples using both picosecond ultrasonics and x-ray reflectivity measurements. The longitudinal sound velocity in the low-frequency range is measured and compared to the predictions of an effective-medium model, including either two or three components per unit cell in order to describe the presence of a mixed interfacial zone. The time-resolved shape of the acoustic response and the reflection coefficient of the substrate are also examined and satisfactorily reproduced using the effective-medium theory.

The evolution of the localized surface mode (LSM) frequency in the first gap (zone boundary) is reported versus multilayer period and compared with theory to solve the disagreement reported in the literature. Buried cavity modes (CMs) are also investigated to distinguish any correlations between bulk or surface modes and microstructure features. Finally, the potential of such Mo/Si stacking for phonon filtering or phonon generation will be illustrated.

## II. EXPERIMENTAL DETAILS AND SAMPLE DESCRIPTION

### A. Sample preparation and physical properties

Mo/Si multilayers were deposited by magnetron sputtering on Si(001) single-crystal substrates covered with a native

oxide layer in a deposition chamber equipped with three independent planar magnetron sources. The standard background pressure in the chamber prior to deposition was $2.0 \times 10^{-6}$ Pa and the Ar sputtering gas pressure during growth was maintained at 0.22 Pa. The deposition was performed at room temperature by alternate sputtering of the Mo (dc voltage of 370 V) and Si target (rf voltage of 460 V). These conditions yield growth rates of 0.072 nm s$^{-1}$ for Mo and 0.067 nm s$^{-1}$ for Si, as calculated from the deposition time and the layer thickness measured by x-ray reflectivity (XRR) on reference samples. Multilayers with periods $d$ ranging from 4.6 up to 28.4 nm were grown, the total thickness being kept constant at a value of $\sim 130$ nm and the Mo thickness ratio $\Gamma = \frac{e_{Mo}}{d}$, where $e_{Mo}$ is the Mo layer thickness and $d$ is the multilayer period at $\Gamma \approx 0.5$. The topmost layer of the stacking was always Si, except for one specific sample. Energy dispersive x-ray analysis (EDX) were performed on multilayers deposited on carbon membranes using a JEOL JSM 5300 microscope operating at 20 keV with a Si(Li) detector in order to determine the composition of all deposited samples. The Mo atomic fraction was found to be $0.54 \pm 0.01$ for all multilayers, which yields a corrected value of the thickness ratio $\Gamma = 0.49 \pm 0.01$ instead of 0.5.

The structural properties of the multilayers were investigated by x-ray diffraction (XRD) using a Bruker D8 Discover diffractometer in Bragg-Brentano geometry. For an accurate determination of layer thickness, x-ray reflectivity measurements were performed on a Seifert XRD 3000 apparatus. For this purpose, the incident beam is formed by a channel cut using two Ge(220) reflections followed by a 0.1 mm slit selecting the Cu K$\alpha_1$ line exclusively with a low divergence; at the exit the 0.07 mm detector slit defines the resolution and as the diffraction circle radius is 220 mm this leads to an acceptance angle below 0.018°.

Finally, cross-section specimen of multilayers were observed using a JEOL 3010 high-resolution transmission electron microscope (HRTEM) equipped with a LaB$_6$ filament and operated at 300 keV, which offers a point resolution of 0.19 nm.

XRD experiments confirm that the Si layers are amorphous for the chosen growth conditions (hereafter, noted $a$-Si) and reveal the (110) textured growth in Mo layers. The thickness of the Mo crystallites, as deduced from the peak width at half maximum and finite-thickness fringes, extends over the whole crystalline Mo layers. The average (110) interplanar spacing, as deduced from a fitting of the diffracted intensity, is slightly reduced as compared to the theoretical value of bulk (110) Mo ($\sim 0.222$ nm instead of 0.225 nm): this difference is possibly explained by the stress state of the thin film or by the incorporation of some residual Si atoms during deposition (the incomplete screening of the Si source during the Mo growth results in a Si content $<3\%$ in the Mo layers). Moreover, it should be mentioned that a structural transition occurs for the Mo layers at a critical thickness of 2.2 nm; below this value Mo layers are amorphous, while they become crystalline over the whole Mo layer thickness as soon as the deposited thickness exceeds this critical value.[14] Needless to mention that here only multilayers with crystalline Mo layers are dealt with.

XRR spectra were acquired in specular $\theta/2\theta$ geometry; information was extracted from the experimental scans by
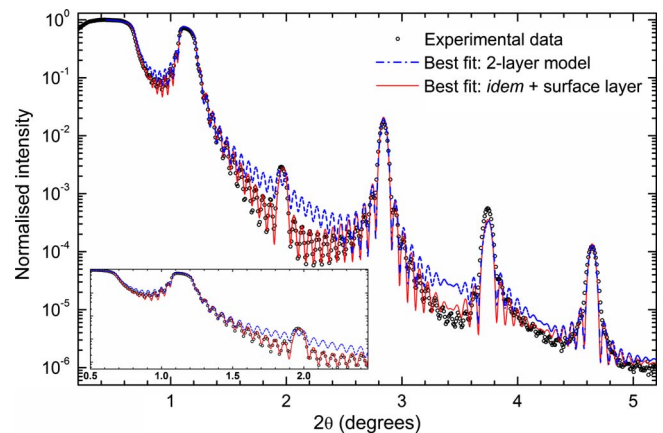


FIG. 1. (Color online) X-ray reflectivity on a 9.6-nm-period Mo/Si multilayer (sample 10a). Symbols: experimental data; dashed line: simulation using the simple two-layer model, the layer density, thickness, and roughness provide the best agreement for the position and amplitude of Bragg peaks; full line: simulation corresponding to the best fit when taking into account a surface silicon oxide layer (thickness $\sim 1.2$ nm) using the same parameters for density, thickness, and roughness as for the dashed line.

comparison to a simulation based on an optical recursion method. XRR analysis provides information on the layer density, layer thickness, and an interfacial broadening parameter for each interface, including both interfacial roughness and/or interdiffusion, as these aspects of interfacial mixing cannot be distinguished in specular geometry. The simulation model used in the Seifert "Analyze" program is based on Parrat's formalism[15] applied on a layered model of the sample: for each layer, the refractive index and the thickness are the relevant parameters; whereas each interface is described by a roughness parameter $\sigma$, the root mean square of the Gaussian distribution of interface height. Moreover, a least-squares fitting procedure using a logarithmic criterion allows the refinement of the layer parameters. Mo/Si multilayers have been studied extensively by several groups,[16–18] and the bilayer model representing the Mo and Si layers was improved to a trilayer model, motivated by the knowledge that there is an interfacial silicide at the Mo-on-Si interface: therefore, a Si/MoSi$_2$/Mo trilayer might be more realistic than the Si/Mo bilayer. However, we found that in our case, the use of a trilayer model does not improve significantly on a simple two-layer model, as on the one hand reflectivity in specular geometry does not allow to distinguish between correlated and uncorrelated roughness and on the other hand the asymmetry of the interfaces can still be taken into account, using different $\sigma$ parameters for Mo-on-Si and Si-on-Mo interfaces. Figure 1 shows the experimental XRR measurement on a 9.6-nm-period multilayer (sample 10a) together with simulated curves. The first simulation uses the simple two-layer model and satisfyingly reproduces the peak positions but not the decay of the intensity at very low angles. However, it is well established that Si layers, especially in the amorphous state, can develop an oxide layer at the Si/air interface, and as a matter of fact, by introducing such a surface oxide layer the agreement between simulation and experimental data can be significantly improved. The effect,

TABLE I. Sample description: $d$ is the multilayer period, $d_1$ (respectively, $d_2$) is the Mo (respectively, Si) thickness in the bilayer, and $\Gamma$ is the thickness ratio of Mo to the period $d$, as determined from XRR analysis. The "sample structure" column gives the number of bilayers together with other specific data. The interfacial parameters $\sigma$ rms (roughness and/or interdiffusion) are given for each type of interface; the values are replaced by—when simulation of the XRR data is not available. The last two columns display the thickness of the topmost Si layer as well as the thickness of the surface oxide layer that forms at the top of it: however, the error on the determination of this latter parameter is quite large ($\sim 0.4$ nm).

| No. | Sample structure | $d$ (nm) | $d_1$ ($e_{Mo}$) (nm) | $d_2$ ($e_{Si}$) (nm) | $\Gamma = e_{Mo}/d$ | $\sigma_{Si\text{-on-Mo}}$ (nm) | $\sigma_{Mo\text{-on-Si}}$ (nm) | Topmost layer (nm) | Surface oxide layer (nm) |
|---|---|---|---|---|---|---|---|---|---|
| | Mo/Si multilayer samples | | | | | | | | |
| 1 | $28^*(a\text{-Si}/\text{Mo})/\text{Si}(100)$ | 4.6 | 2.2 | 2.4 | 0.47 | 0.7 | 1.1 | 2.4 | 1.1 |
| 2 | $19^*(a\text{-Si}/\text{Mo})/\text{Si}(100)$ | 6.3 | 3 | 3.3 | 0.48 | 0.65 | 0.95 | 3.3 | 1.4 |
| 3 | $13^*(a\text{-Si}/\text{Mo})/\text{Si}(100)$ | 9.3 | 4.6 | 4.6 | 0.50 | 0.6 | 0.8 | 4.6 | 1.4 |
| 4a | $10^*(a\text{-Si}/\text{Mo})/\text{Si}(100)$ | 12 | 6 | 6 | 0.50 | 0.65 | 0.8 | 6 | 1.4 |
| 4b | $\text{Mo}+10^*(a\text{-Si}/\text{Mo})/\text{Si}(100)$ | 12 | 6 | 6 | 0.50 | 0.65 | 0.8 | (Mo) | 1.4 |
| 5 | $8^*(a\text{-Si}/\text{Mo})/\text{Si}(100)$ | 15 | 7.3 | 7.7 | 0.49 | 0.8 | 0.9 | 7.7 | 1.4 |
| 6 | $9^*(a\text{-Si}/\text{Mo})/\text{Si}(100)$ | 18.9 | 9.2 | 9.6 | 0.49 | 0.7 | 0.8 | 9.6 | 1.2 |
| 7 | $8^*(a\text{-Si}/\text{Mo})/\text{Si}(100)$ | 23.8 | 11.7 | 12.1 | 0.49 | 0.7 | 1.2 | 12.1 | 1 |
| 8 | $8^*(a\text{-Si}/\text{Mo})/$ | 28.4 | 13.5 | 14.9 | 0.48 | 0.75 | 0.95 | 14.9 | 1.4 |
| | Mo cavity samples | | | | | | | | |
| 9a | $a\text{-Si}+2^*(\text{Mo}/a\text{-Si})/\text{Mo}\ 5.73\ \text{nm}/3^*(a\text{-Si}/\text{Mo})/\text{Si}(100)$ | 12 | 2.6 | 9.4 | 0.22 | | | | |
| 9b | $2^*(\text{Mo}/a\text{-Si})/\text{Mo}\ 5.73\ \text{nm}/3^*(a\text{-Si}/\text{Mo})/\text{Si}(100)$ | 12 | 2.6 | 9.4 | 0.22 | | | | |
| | Modified topmost Si layer | | | | | | | | |
| 10a | $13^*(a\text{-Si}/\text{Mo})/\text{Si}(100)$ | 9.6 | 5 | 4.6 | 0.52 | 0.6 | 0.8 | 4.6 | 1.6 |
| 10b | $\text{Si-2}\ \text{nm}/\text{Mo}/12^*(a\text{-Si}/\text{Mo})/\text{Si}(100)$ | 9.6 | 5 | 4.6 | 0.52 | 0.7 | 0.9 | 2.6 | 1.5 |
| 10c | $a\text{-Si}+1.5\ \text{nm}/\text{Mo}/12^*(a\text{-Si}/\text{Mo})/\text{Si}(100)$ | 9.6 | 5 | 4.6 | 0.52 | 0.7 | 0.9 | 6.0 | 1.6 |
| | Generation and detection samples | | | | | | | | |
| 11 | $3^*(a\text{-Si}/\text{Mo})/\text{Si}(100)\ 260\ \mu\text{m}/\text{Al}\ 30\ \text{nm}$ | 25 | 12.5 | 12.5 | 0.50 | | | | |
| 12 | $\text{Si}/\text{Mo}/\text{Si}\ 21.6\ \text{nm}/\text{Mo}/\text{Si}/\text{Mo}/\text{Si}(100)260\ \mu\text{m}/\text{Al}\ 30\ \text{nm}$ | 16 | 8 | 8 | 0.50 | | | | |

when taking into account a silicon oxide surface layer with a slightly lower density ($\sim 2$ g cm$^{-3}$) than the one of the actual Si layer (2.33 g cm$^{-3}$), is visible especially in the low-angle region (inset of Fig. 1). Using the two-layer model and the Si oxide surface layer the thicknesses of the individual dense (Mo) and light (Si) layers were determined for all multilayers: the accuracy on the multilayer period is on the order of 0.01 nm. The experimental spectra are not shown here, as the results were similar to the one shown in Fig. 1. An asymmetry of the interface profile (roughness and/or interdiffusion) is obvious and consistent throughout the series of samples, yielding a $\sigma$ parameter of $\sim 1.0$ nm rms for the Mo-on-Si interface, while it is only of about 0.7 nm rms for the Si-on-Mo interface. The presence of a modified surface layer was taken into account for all samples: however, the precision on the thickness determination of such a surface oxide layer is very poor.

HRTEM observations of the samples confirmed the strong asymmetry of the interfaces with the existence of an amorphous silicide interfacial layer extending over up to $\sim 2$ nm at the Mo-on-Si interface, whereas the Si-on-Mo interface is mainly subject to roughness. It should be mentioned that these observations are in good agreement with several previous studies on the Mo/Si system, which always point out an

interfacial diffusion and the possible creation of an amorphous alloyed layer with a rather well-defined stoichiometry of $\text{Mo}_{0.33}\text{Si}_{0.67}$.[17]

The main structural characteristics of the samples are summarized in Table I. In particular, the good agreement between XRR and EDX analysis for the determination of the thickness ratio $\Gamma$ should be mentioned: a point that tends to prove that the two-layer model that was employed is appropriate.

### B. Picosecond ultrasonics

The picosecond ultrasonics technique introduced by H. Maris[19] derives from the well-known optical pump-and-probe scheme. A femtosecond laser pulse (the pump beam) is absorbed at the sample surface. This absorption generates, by thermal-expansion, acoustic waves which propagate through the system. Partly reflected and transmitted at all the interfaces of the sample, the acoustic wave is then probed at the free surface by a time-delayed laser pulse called the probe beam, which is less energetic than the excitation beam. The real and imaginary parts of the relative change in surface reflectivity ($\Delta r / r$) induced by such acoustical strain may be measured either by reflectivity[20–22] or by interferometric
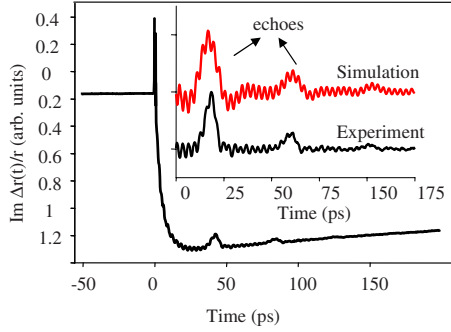
FIG. 2. (Color online) Standard time-resolved picosecond acoustics reflectivity measurement using a Michelson interferometer on a 9.3-nm-period Mo/Si multilayer (sample 3). The fast oscillations starting just right after the pump excitation absorption are the signatures of the LSMs. Low-frequency acoustic waves reflected by the silicon substrate emerge at the sample surface periodically. The inset shows a comparison between experimental data and results obtained by a simulation based on the transfer-matrix formalism.

measurements.[23–27] Our experimental setup working either in reflection[27,28] or in transmission geometry[29] was already described elsewhere. Briefly, we use a mode-locked Ti:Sapphire (MAI-TAI Spectra) laser source operating at 800 nm with a repetition rate around 79.3 MHz. The pulse time width is less than 100 fs at the laser output. The pump beam is modulated at 1.8 MHz to improve the signal-to-noise ratio. After traveling through a delay line the probe beam is focused at the location of the pump excitation beam and its reflection is detected by a photodiode connected to a lock-in amplifier. For measurements at room temperature a Michelson interferometer is used; at low temperature a Sagnac[30] configuration is mandatory since it is less sensitive to optical disturbances induced by the helium flow in the cryostat cell.

In the following, we will consider a one-dimensional elastic model to account both for the generation and detection processes, as the laser spot size is wider than the characteristic lengths of all related phenomena (thermal diffusion length, optical-absorption length...).

## III. RESULTS AND DISCUSSION

### A. Low-frequency acoustic waves and effective-medium model

Figure 2 displays the imaginary part of the reflectivity variation $\Delta r(t)/r$ induced by the acoustic waves into a 9.3-nm-period Mo/Si multilayer. The time $t=0$ corresponds to a sharp response of the electrons in the system. After a few picoseconds, the absorbed energy is transferred to the lattice, giving rise to a smooth thermal background. The acoustical features are superimposed onto this signal. The broad structures correspond to the echoes separated by a constant time delay as in a standard sonar system. For such low-frequency modes, the main interest of the interferometry is to be sensitive to acoustic waves, which have traveled through the whole multilayer structure and back after reflection at the interface with the silicon substrate. The imaginary part of $\Delta r(t)/r$ although partly correlated with the surface displace-

TABLE II. Parameters determined for the pure thin films reference: volumic mass $\rho$ and longitudinal sound velocity $V$.

| Reference sample | $\rho$ (g cm$^{-3}$) | $V$ (nm ps$^{-1}$) |
|---|---|---|
| $a$-Si | 2.33 | 7.56 |
| Mo | 10.2 | 6.18 |
| Mo$_{0.33}$Si$_{0.67}$ | 5.5 | 6.68 |

ment is generally more sensitive to acoustic waves with a wavelength longer than the optical penetration depth (a few tens of nm).

In layered structures, the transfer-matrix formalism is adequate for the calculation of the acoustic wave propagation and induced reflectivity. The generation process is then considered as the sum of multiple strain sources due to the absorption of light in different layers, and the detection process is related to the optical penetration depth of the light probe. In the inset of Fig. 2 a comparison between calculated and experimental values for the imaginary part of the reflectivity variation is shown. The acoustical response includes fast oscillations with a slow damping rate, a signature of vibrations located close to the free surface (the so-called localized surface modes), and additional broad structures. The nonpropagating localized surface modes will be discussed in Sec. III B of the paper.

As shown in Fig. 2, the bulk waves exhibit characteristic pulse duration around 10 ps, which correspond to a typical wavelength of one order of magnitude larger than the sample periodicity. Consequently, we may assume that such waves propagate in an effective medium.

The effective-medium model predicts an effective elastic constant $C_{33}$ for the superlattice given by

$$\frac{d}{C_{33}} = \sum_i \frac{d_i}{C_{33}^i}, \qquad (1)$$

where $d$ is the multilayer period and $d_i$ and $C_{33}^i$ are, respectively, the thickness and the elastic constant of $i$th layer constituting the elementary cell of the periodic structure.

A preliminary step for applying Eq. (1) is the determination of the sound velocity and density for $a$-Si and for (110) textured Mo reference thin films grown in the same conditions as the multilayer samples as they might differ from the bulk values. The corresponding values are summarized in Table II. The effective elastic constant $C_{33}$ of the multilayers is obtained from the average time delay between several echoes (Fig. 2) and assuming that the density of the multilayer obeys a simple rule of mixture $\rho = \frac{d_1\rho_1 + d_2\rho_2}{d}$.

Figure 3 shows the measured effective elastic constants compared to the values calculated for an effective-medium model, including only the two components Mo and Si. A good agreement is achieved between experimental values and the effective model prediction as the maximum difference is less than 3.5%. Even for the smallest multilayer periods, which are the most sensitive to interfacial effects, no significant divergence from the model is observable. Nevertheless, keeping in mind the possible presence of an interfa-
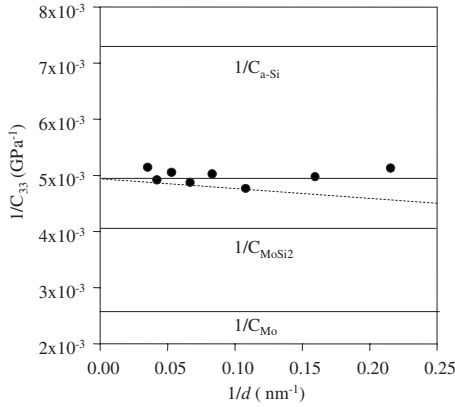
FIG. 3. Evolution of the effective longitudinal elastic constant $C_{33}$ vs multilayer period in reciprocal scale. Black dots: experimental data. The size of the dots represents the experimental error. Continuous line: calculated values in a two-component model including equal-thickness Mo and $a$-Si layers in the unit cell; dashed line: calculated values using a three-component model, namely, Mo, $Mo_{0.33}Si_{0.67}$, and $a$-Si layers in the unit cell. The measured effective elastic constants of the elementary constituents Mo and $a$-Si are also indicated.

cial alloy with a composition close to $Mo_{0.33}Si_{0.67}$ at the interface, an elastic constant calculated using the effective-medium model based on a cell composed by three elementary constituents $(Mo/MoSi_2/Si)$ is also included in Fig. 3. For these calculations, the properties of an amorphous $Mo_{0.33}Si_{0.67}$ alloy were measured independently on a reference specimen and the alloy thickness was fixed at a value of $\sim 2$ nm, as derived from HRTEM image analysis.

Eventually, as Fig. 3 confirms, taking into account the interfacial layer in the model does not improve the agreement to the experimental data; on the contrary, this leads to a slight hardening at low multilayer periods. However, the existence of an amorphous interfacial layer was established by HRTEM observations: we then have to assume that either such an interfacial layer does not follow the behavior of the corresponding higher-thickness reference sample or the expected interfacial hardening effect is counterbalanced by another effect. Again based on HRTEM observations, it may be inferred that the roughness at the Si-on-Mo interface induces an elastic softening. In any case, the experimental effective sound velocity in Mo/Si multilayers is satisfactorily reproduced by the two-constituent model.

Using the signature of consecutive echoes, we can extract another acoustic parameter, which is related to the interface between the Mo/Si stacking and the silicon substrate. Indeed, each acoustic echo detected at the free surface undergoes at least one reflection at that interface. Assuming a perfect adhesion and neglecting sound absorption, the reflection coefficient of the acoustic waves has been deduced from the amplitude decay of the first three echoes. This reflection coefficient determination was applied mainly for the sample with smallest period (sample 1) as the effective-medium assumption is here the most adequate. The experimental value was found to be around 0.30, in good agreement with the expected value of 0.27 calculated using the sound velocity and density measured on the pure Mo and $a$-Si reference

films. As can be noted in Fig. 2, for the sample with $d$ =9.6 nm, the amplitude decay of the echoes is well reproduced with a reflection coefficient of about 0.30 also for samples with larger periods.

The assumption of effective-medium behavior, which has been shown to be adequate for describing the amplitude and time delay of the echoes, can also be tested on the shape of the first echo.

In the effective-medium model, and assuming that generation and detection take place in an opaque and homogeneous layer, the relative variation in the reflectivity is given by the following equation[23]
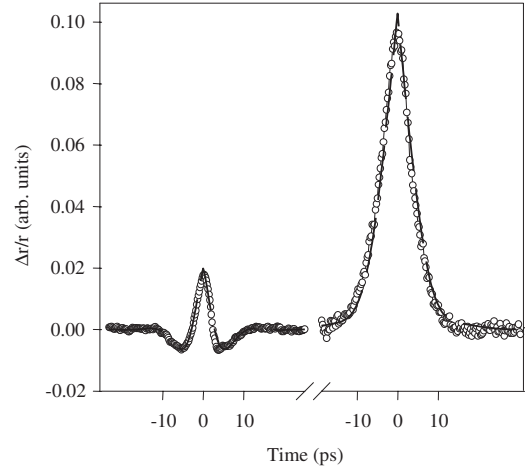


FIG. 4. Real and imaginary parts of the relative change in reflectivity induced at the first echo in the 4.6-nm-period Mo/Si multilayer (sample 1). Open circles: real part of the relative change in reflectivity on the left side and imaginary part on the right side. Dashed line: results of the fitting with an effective model for the echo shape.

$$\frac{\Delta r}{r} = -\frac{\eta_0 r_0}{n''} e^{-\alpha v |t|} \left\{ i + \gamma e^{i\theta} \left[ \left( \frac{n'}{n''} + i \right) e^{i\xi\alpha v |t|} - i \right] \right\} \quad (2)$$

with the sound velocity $v$, the photoelastic coefficient $\frac{\partial n}{\partial \eta}$, and the optical index $n = n' + in''$, $\alpha = 4\pi n''/\lambda$, and $\gamma e^{i\theta} = \frac{2nn''^2}{n'(1-n^2)(2n-n')} \frac{\partial n}{\partial \eta}$.

Full information on this complex quantity can be obtained using both interferometric and reflectivity measurements; the real and imaginary parts of the reflectivity induced at the first echo in sample 1 are displayed in Fig. 4. The experimental data were fitted with the aid of Eq. (2) using a least-squares method. A good agreement between model and experiment was found with an effective optical index of $n = 5.2 + 3.4i$ and a photoelastic coefficient $1.1 - 1.2i$.

As a conclusion, the overall good agreement between experimental results and effective-medium model predictions covers all acoustic features: sound velocity, sound reflection, amplitude, and shape of the acoustic echo. This is a strong support to the fact that the properties of the two constituent layers in the Mo/Si system are well understood and determined accurately enough to reproduce adequately the low-frequency behavior of Mo/Si multilayers. Moreover, the
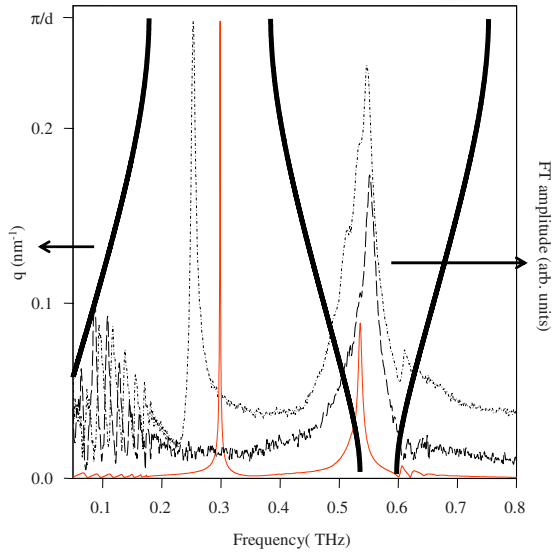
FIG. 5. (Color online) Thick line: (*frequency wave-vector diagram*) dispersion curve in an infinite multilayer with a period *d* =12 nm and a thickness ratio $\Gamma=0.5$. Note the large stop band at the BZ boundary. Dashed line: (*frequency Fourier transform amplitude diagram*) experimental spectra obtained for a sample with topmost Si layer (sample 4a, dash-dotted curve) and with topmost Mo layer (sample 4b, dashed curve), respectively. The LSM disappears when the topmost layer has the higher acoustical impedance. Fine red line: calculated spectrum using transfer-matrix formalism; the predicted surface mode frequency is systematically higher than the experimental value.

presence of an alloyed Mo/Si interface was clearly not detectable from the low-frequency acoustic behavior.

### B. High-frequency range: Localized surface modes

One of the main targets of the above-mentioned effective-medium model focused on the low-frequency multilayer response was to obtain realistic acoustic parameters for Mo and Si layers with thicknesses in the nanometer scale without referring to their bulk properties. These parameters being determined, they can now be used for a better understanding of the high-frequency features.

In a superlattice the layers stacking periodicity in the direction perpendicular to the layers modifies deeply the propagation of acoustic phonons, leading to the backfolding of the acoustic dispersion into minibranches in the Brillouin zone (BZ) and the opening of energy gaps in the Brillouin-zone center and boundary. For these energies, no propagating modes are allowed and superlattices behave as Bragg mirrors with an efficiency determined by the number of periods and the acoustic impedance contrast between the two constituents. Surface-localized modes can be confined in superficial layers of the mirror since the interface with air is a perfect reflector provided that the topmost layer has the smallest acoustic impedance. An acoustic cavity can also be obtained if any layer is sandwiched between two such mirrors, leading to a so-called cavity mode centered on the cavity layer.

We show in Fig. 5 the dispersion curve obtained for a period *d*=12 nm and a thickness ratio $\Gamma=0.5$, which corre-

sponds to samples 4a and 4b, which only differ by the nature of the topmost layer of the sample being either Mo or Si. For a constant thickness ratio Mo:Si close to 1:1, the first band gap is the largest at the Brillouin-zone boundary. The frequency width of the stop band is directly related to the acoustical impedance contrast of the two constituents. In our case, the very large stop bandwidth (wider than 200 GHz) is mainly due to the higher Mo density as compared to the Si one. For comparison, in semiconductor superlattice systems such as GaAs-AlAs,[7] the stop band does not exceed a width of 10 to 20 GHz. Such properties of metal-semiconductor multilayers may be in the future a real advantage for tailoring specific filter devices.

After subtracting the decreasing background due to thermal and electronic effects in the reflectivity change we performed a Fourier transform to get the acoustic spectrum response of the multilayer. The result obtained on samples 4a and 4b are shown in Fig. 5.

The sharp peak observed within the band gap (at ∼250 GHz) is related to nonpropagating localized surface modes. It is well known that such modes can exist only if the topmost layer has acoustical impedance smaller than the underlying layer one. Consequently, the spectrum on sample 4b (topmost layer Mo) does not show any structure within the first band gap. The second structure, which is wider, is attributed to a band of folded modes in the vicinity of the almost-closed Brillouin-zone-center gap. Both localized surface modes and folded modes frequencies increase when the multilayer period decreases. In semi-infinite multilayers, the frequency position of the localized surface modes satisfies the equation[20]

$$\tan\left(\frac{2\pi f d_2}{c_2}\right) + \frac{\rho_1 c_1}{\rho_2 c_2}\tan\left(\frac{2\pi f d_1}{c_1}\right) = 0, \qquad (3)$$

where $d_i$, $\rho_i$, and $c_i$ are the thicknesses, densities, and longitudinal sound velocities of the constituents (*i*=1 for Si and *i*=2 for Mo). Thus the surface-localized frequency should vary as the inverse of the period while keeping the same thickness ratio.

In Fig. 6 the plot of the localized surface mode frequency versus the inverse of the superlattice period is shown. The results are in rough agreement with the expected linear evolution but a substantial discrepancy between the theoretical and experimental values is obvious especially for the smallest multilayer periods, as already reported in the literature.[10,11] As in the effective-medium model, the possibility of the influence of an interfacial alloy on the frequency value of the surface modes was investigated. Nevertheless, the influence of an amorphous interfacial alloy on the localized surface modes is to produce a frequency shift in only a few GHz, which is insufficient to explain the discrepancy observed in Fig. 6. In fact, this is not surprising and may be explained by a strong confinement of such acoustic vibrations at the vicinity of the surface. Then, buried structures have no significant influence on the localized surface mode frequency. On the contrary, the vibrational response would exhibit a very strong correlation to the thickness of the topmost Si layer. Such an effect might be considered as it has been shown that the formation of a silicon surface oxide is
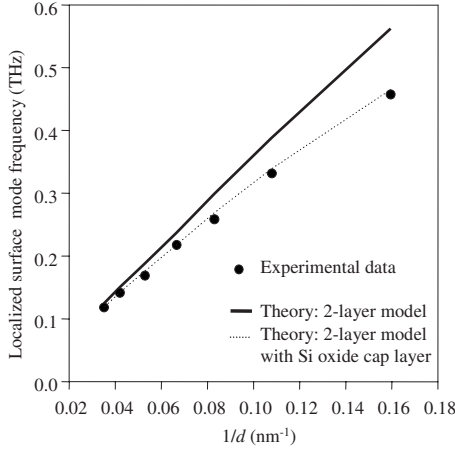
FIG. 6. Evolution of the surface mode frequency vs inverse of the period. Black dots: experimental data; bold line: calculated values in a simple two-constituents Mo and Si, model; dashed line: calculated values with the same model but taking into account an additional 1-nm-thick Si surface layer.

not negligible in these multilayer samples, and it actually leads to an additional oxide "cap layer" on top of the topmost Si layer (see Table I). In order to validate this assumption, three identical multilayers with different thicknesses of the topmost Si layer were grown (samples 10a, 10b, and 10c), and Fig. 7 presents the corresponding experimental power spectra. As expected we observe a shift to the low frequencies for samples having the thickest silicon topmost layer.

Such high sensitivity of the localized surface mode frequency to the topmost layer thickness has been explained by Chen *et al.*[31] through the following equation

$$
\begin{aligned}
&\sin(\alpha_{cap}) * \cos(\alpha_{cap}) * \sin(\alpha_1) * \sin(\alpha_2) * (r - 1/r) \\
&\quad + \cos(\alpha_{cap})^2 * [r * \sin(\alpha_1) * \cos(\alpha_2) + \sin(\alpha_2) * \cos(\alpha_1)] \\
&\quad + \sin(\alpha_{cap})^2 * [\sin(\alpha_1) * \cos(\alpha_2)/r + \sin(\alpha_2) * \cos(\alpha_1)] \\
&\quad = 0
\end{aligned}
\tag{4}
$$

with $\alpha_i = \frac{2\pi f d_i}{c_i}$, where $d_i$, $\rho_i$, and $c_i$ are the thicknesses, densities, and longitudinal sound velocities of the constituents (in that case $i=1$ for Mo and $i=2$ for Si, and $i=cap$ corresponds to the topmost Si layer), and $r$ is the ratio of the acoustical impedance of Mo on the one of Si.

In the case illustrated in Fig. 7, where the ratio between the layer thicknesses is equal to one, we get a maximum shift in frequency versus the topmost layer thickness.

In order to obtain structural data about these multilayers, the same set of samples was studied using XRR and the corresponding data for samples 10b and 10c are shown in Fig. 8. Here again, the small change in the topmost Si layer has clear effects on the experimental spectrum, especially at the very low angles. The best fit between simulation and data is obtained when the topmost Si layer thickness is decreased by 2 nm (respectively increased by 1.4 nm) compared to the reference multilayer, in perfect agreement with the nominal values, but taking into account the surface oxide cap layer. This comparative study on a series of very similar samples
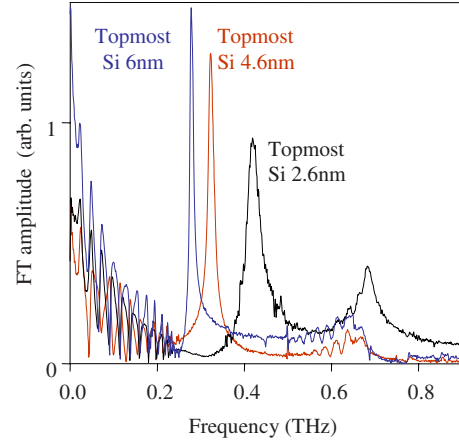


FIG. 7. (Color online) Spectra measured on three identical multilayers for which only the topmost Si layer has been modified. The multilayer period is $d=9.6$ nm, and the topmost layer thickness is 6.0 (blue), 4.6 (red), and 2.6 nm (black) (samples 10c, 10a, and 10b, respectively).

confirms that a careful analysis of the XRR spectra can detect such small surface layer thickness variations although they are at the sensitivity threshold of the technique. At this purpose picosecond acoustics measurement seems to present a better sensitivity compared to x-ray reflectivity.

These observations coupled with the accurate prediction of the position of the broad folded mode bands in the zone-center gap (Fig. 5) lead to the conclusion that the acoustic behavior of Mo/Si multilayers is well reproduced with the exception of the acoustic vibrations located on the surface. In order to investigate this point further, we designed specific Mo/Si multilayered structures including a buried Mo cavity. In the present case, the thickness of Mo and Si layers ($\Gamma = 0.22$) have been chosen to open a band gap in the boundary
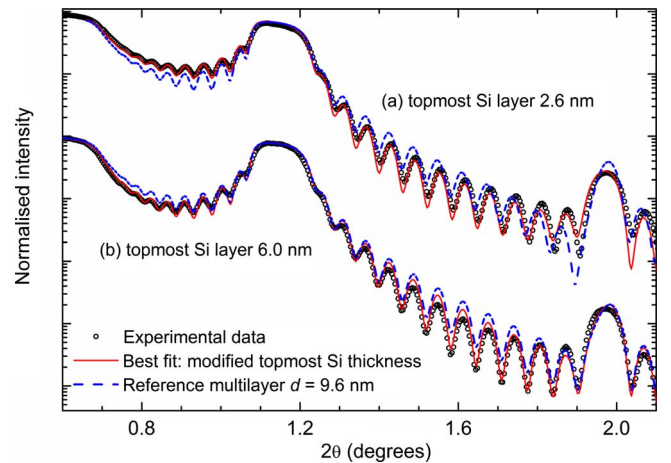


FIG. 8. (Color online) X-ray reflectivity on identical multilayers for which only the topmost silicon layer thickness has been modified (samples 10c and 10b). The multilayer period is 9.6 nm and the topmost layer thickness is (a) 2.6 nm and (b) 6.0 nm. The best fit simulations were obtained for the modified topmost layer thickness, while always keeping the same surface oxide "cap layer." Also, for comparison, the spectrum for the reference multilayer without surface layer modification is given.
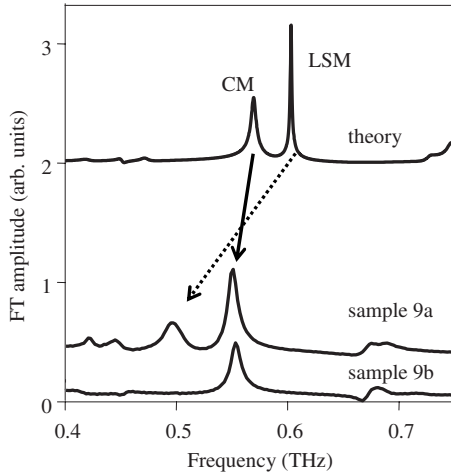
FIG. 9. Bottom: experimental spectra for structures with buried Mo cavities (sample 9a with topmost Si layer and sample 9b with topmost Mo layer). Top: corresponding calculated power spectrum, the LSM frequency is 604 GHz and the Mo CM frequency is 569 GHz. The agreement between theory and experiment is satisfying for the CM (experimental value 550 GHz), whereas for the LSM frequency the experimental value (497 GHz) is much lower than the prediction, a discrepancy of around 17%.

and in the center of the Brillouin zone, then localized surface modes at least in the two first band gaps are observed. The experimental spectrum around the second stop band is compared to the calculated spectrum in Fig. 9. In order to unambiguously distinguish the localized surface mode signature from the signal originating from the Mo cavity, we have compared two otherwise identical stacking with either Si or Mo topmost layer (samples 9a and 9b, respectively). As previously mentioned, for a Mo topmost layer the localized surface modes disappear, leaving only the cavity mode signal. As compared to simulations, a shift toward lower frequencies for the surface-localized modes is visible. On the contrary, the experimental resonance frequency of the buried Mo cavity is very close to the predicted one as the difference is less than 4%.

For these reasons, it is clear that the disagreement reported in Fig. 6 can definitely not be attributed to incorrect elastic and structural parameters determination. Hence, the main contribution to the localized surface modes' frequency shift must be related to the surface or topmost layer properties. Figure 6 also displays the predicted frequency values calculated when taking into account an additional silicon surface layer of 1 nm thickness for the whole series of multilayers. In the latter case, a nearly perfect agreement with the experimental values is obtained. It should be emphasized that this modification of the topmost silicon layer consistent with the acoustic surface modes is in full agreement with x-ray reflectivity analysis (Table I).

Finally, we achieved a very consistent description of the acoustic properties of these Mo/Si multilayers both in the low and the high-frequency ranges. Consequently, it is now possible to tailor active or passive sensors in order to manipulate phonons.
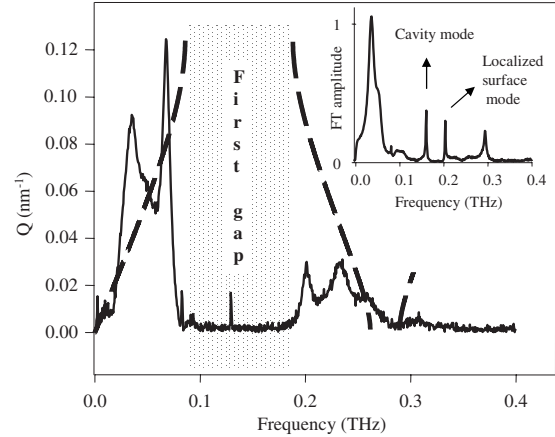


FIG. 10. Acoustic transmission spectroscopy at low temperature (15 K) obtained for a $d=25$ nm period multilayer mirror deposited on a 260 $\mu$m Si substrate (sample 11): there is no transmission in the first band gap except at the LSM frequency. Inset: transmission of the sample containing a Si cavity (sample 12), same trend with an additional selective transmission located at the CM frequency.

### C. Potential applications of large band-gap structures

Recently it has been shown that semiconductor superlattices have a great potential for monochromatic acoustic wave generation or detection.[8,32] Such properties coupled with their optical and electrical behaviors correspond to a large window of industrial applications in the range of subterahertz to terahertz phonon manipulation. Mo/Si multilayers could be an alternative system to produce passive or active devices as their growth is not limited by epitaxial conditions as for semiconductor systems. To illustrate the validity of this argument, we additionally performed acoustic transmission spectroscopy.

In a first configuration we investigate the detection properties of the multilayer: the pump beam is focused on an Al film deposited on the backside of the silicon substrate, which is used as a coherent broadband phonon generator. The generated acoustic pulse, containing frequencies up to 0.35 THz, propagates through the substrate before reaching the multilayer where the probe beam is focused on. In order to prevent acoustic attenuation in the 260 $\mu$m-thick Si substrate, the sample is cooled down to 15 K. The transmitted signal detected on a 25-nm-period multilayer (sample 11) is shown in Fig. 10: between 0.09 and 0.18 THz an opening can be observed into the transmitted spectrum corresponding to the first gap induced by the sample periodicity. The acoustic waves within that frequency range are totally reflected by the Mo/Si multilayer stacking, demonstrating a huge filtering efficiency even for a small number of periods (only three repetitions). Within the stop band we can observe a sharp peak related to the excitation of the surface-localized mode by tunneling through the stacking. For the sample containing a Si cavity (sample 12), we also observe a selective filtering at the cavity frequency mode as shown in the inset of Fig. 10.

In a second configuration, we aim to observe the generation properties of the same Mo/Si samples by reversing the experimental geometry. Now the pump excitation is directly absorbed in the superlattice and we measure the acoustic
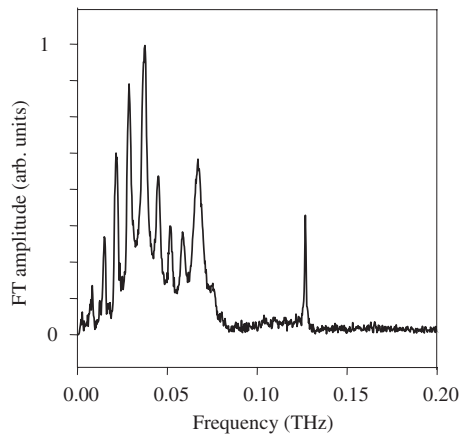
FIG. 11. Acoustic generation spectrum from a $d=25$ nm multilayer mirror deposited on a 260 $\mu$m Si substrate detected through a backside Al layer (sample 11). The broadband of the low-frequency branch stops abruptly at the first band gap. The well-defined peak at about 130 GHz is induced by the tunneling of the surface mode across the multilayer stack.

response at the opposite side by measuring the change in the reflected probe, which is focused on the aluminum film. In the case of a multilayer mirror system (sample 11), the Fourier transform of the reflectivity change is shown in Fig. 11. At low frequencies, a broadband appears in the spectrum, corresponding to the low-frequency branch of the dispersion curve. The spectrum is then abruptly cut at the low-frequency edge of the first gap (80 GHz). An additional sharp structure emerges into the gap (at 127 GHz) and corresponds

to the localized surface mode vibration excited by the pump pulse and which tunnels through the multilayer up to the substrate. This generation process is also observed in the systems containing a phonon cavity. These preliminary results support the assumption that Mo/Si multilayers grown by magnetron sputtering are adequate as detectors or generators at least in the range of 100 to 200 GHz.

## IV. CONCLUSION

In this paper we have investigated microstructural and acoustic properties of Mo/Si multilayers. In the low-frequency range the elastic behavior of Mo/Si multilayer is well explained by an effective model, including only two layers into the periodic cell and using elastic and structural parameters deduced from measurements performed on pure reference Mo and $a$-Si single-layer thin films deposited in the same conditions. The high-frequency response including localized surface mode or cavity modes has also been studied. The frequency of buried cavity structures are well reproduced using the nominal multilayer thickness, whereas the localized surface mode frequency is systematically lower than the predicted value. We have explained this discrepancy by an increase in the topmost Si layer thickness due to an oxide cap layer, which is in agreement with x-ray reflectivity analysis. Finally, the potential of such layered structures for phonon filtering, generation, or detection has also been evidenced. In the near future, such versatile multilayer systems could be used to study the phonon propagation into a very large panel of systems even in the higher-frequency range provided that there is a better control on the interface quality.

*Author to whom correspondence should be addressed. laurent.belliard@upmc.fr

[1] C. Colvard, R. Merlin, M. V. Klein, and A. C. Gossard, Phys. Rev. Lett. **45**, 298 (1980).

[2] H. T. Grahn, H. J. Maris, and J. Tauc, IEEE J. Quantum Electron. **25**, 2562 (1989).

[3] C. Rossignol, B. Perrin, B. Bonello, P. Djemia, P. Moch, and H. Hurdequint, Phys. Rev. B **70**, 094102 (2004).

[4] R. S. Rosen, D. G. Stearns, M. A. Viliardos, M. E. Kassner, S. P. Vernon, and Y. Cheng, Appl. Opt. **32**, 6975 (1993).

[5] N. M. Ceglio, D. G. Stearns, D. P. Gaines, A. M. Hawryluk, and J. E. Trebes, Opt. Lett. **13**, 108 (1988).

[6] J. E. Bjorkholm, J. Bokor, L. Eichner, R. R. Freeman, J. Gregus, T. E. Jewell, W. M. Mansfield, A. A. MacDowell, E. L. Raab, W. T. Silfvast, L. H. Szeto, D. M. Tennant, W. K. Waskiewicz, D. L. White, D. L. Windt, O. R. Wood II, and J. H. Bruning, J. Vac. Sci. Technol. B **8**, 1509 (1990).

[7] J. A. Trail and R. L. Byer, Opt. Lett. **14**, 539 (1989).

[8] A. Huynh, N. D. Lanzillotti-Kimura, B. Jusserand, B. Perrin, A. Fainstein, M. F. Pascual-Winter, E. Peronne, and A. Lemaitre, Phys. Rev. Lett. **97**, 115502 (2006).

[9] M. B. Stearns, C.-H. Chang, and D. G. Stearns, J. Appl. Phys. **71**, 187 (1992).

[10] N. W. Pu and J. Bokor, Phys. Rev. Lett. **91**, 076101 (2003).

[11] N. W. Pu, J. Bokor, S. Jeong, and R.-I. Zhao, Appl. Phys. Lett. **74**, 320 (1999).

[12] N. W. Pu, J. Bokor, S. Jeong, and R.-I. Zhao, J. Vac. Sci. Technol. B **17**, 3014 (1999).

[13] W. Kuo, E. Y. Pan, and N. W. Pu, J. Appl. Phys. **103**, 093533 (2008).

[14] S. Bajt, D. G. Stearns, and P. A. Kearney, J. Appl. Phys. **90**, 1017 (2001).

[15] L. G. Parrat, Phys. Rev. **95**, 359 (1954).

[16] A. K. Petford-Long, M. B. Stearns, C. H. Chang, S. R. Nutt, D. G. Stearns, N. M. Ceglio, and A. M. Hawryluk, J. Appl. Phys. **61**, 1422 (1987).

[17] J. M. Slaughter, D. W. Schulze, C. R. Hills, A. Mirone, R. Stalio, R. N. Watts, C. Tarrio, T. B. Lucatorto, M. Krumrey, P. Mueller, and C. M. Falco, J. Appl. Phys. **76**, 2144 (1994).

[18] C. Largeron, E. Quesnel, and J. Thibault, Philos. Mag. **86**, 2865 (2006).

[19] C. Thomsen, H. T. Grahn, and H. J. Maris, Phys. Rev. B **34**, 4129 (1986).

[20] H. T. Grahn, H. J. Maris, J. Tauc, and B. Abeles, Phys. Rev. B **38**, 6066 (1988).

[21] B. Perrin, B. Bonello, J. C. Jeannet, and E. Romatet, Prog. Nat. Sci. **S6**, 444 (1996).

[22] O. B. Wright and T. Hyoguchi, Opt. Lett. **16**, 1529 (1991).

[23] B. Perrin, C. Rossignol, B. Bonello and J.-C. Jeannet, Physica B **263-264**, 571 (1999).

[24] Y. Sugawara, O. B. Wright, O. Matsuda, and V. E. Gusev, Ultrasonics **40**, 55 (2002).

[25] C. Rossignol, B. Perrin, S. Laborde, L. Vandenbulcke, M. I. Barros, and P. Djemia, J. Appl. Phys. **95**, 4157 (2004).

[26] G. A. Antonelli, B. Perrin, B. C. Daly, and D. G. Cahill, MRS Bull. **31**, 607 (2006).

[27] T. Bienville, J.-F. Robillard, L. Belliard, I. Roch-Jeune, A. Devos, and B. Perrin, Ultrasonics **44**, e1289 (2006).

[28] T. Bienville, L. Belliard, P. Siry, and B. Perrin, Superlattices Microstruct. **35**, 363 (2004).

[29] F. Decremps, L. Belliard, B. Perrin, and M. Gauthier, Phys. Rev. Lett. **100**, 035502 (2008).

[30] J.-Y. Duquesne and B. Perrin, Phys. Rev. B **68**, 134205 (2003).

[31] W. Chen, Y. Lu, H. J. Maris, and G. Xiao, Phys. Rev. B **50**, 14506 (1994).

[32] N. D. Lanzillotti-Kimura, A. Fainstein, A. Huynh, B. Perrin, B. Jusserand, A. Miard, and A. Lemaitre, Phys. Rev. Lett. **99**, 217405 (2007).